Inorganic Chemistry

Article

pubs.acs.org/IC

Thermal- and Light-Induced Spin-Crossover Bistability in a Disrupted Hofmann-Type 3D Framework

Natasha F. Sciortino,[†] Suzanne M. Neville,[†] Jean-François Létard,[‡] Boujemaa Moubaraki,[§] Keith S. Murray,[§] and Cameron J. Kepert*[,†]

[†]School of Chemistry, The University of Sydney, Sydney, New South Wales 2006, Australia

[‡]Laboratoire des Sciences Moléculaires, ICMCB (CNRS UPR 9048), Université Bordeaux I, 33608 Pessac, France

[§]School of Chemistry, Monash University, Clayton, Victoria 3800, Australia

Supporting Information

ABSTRACT: The expected 3D and 2D topologies resulting from combining approximately linear bis- or monopyridyl ligands with $[Fe^{II}M^{II}(CN)_4]$ (M^{II} = Pt, Pd, Ni) 4,4-grid sheets are well established. We show here the magnetic and structural consequences of incorporating a bent bispyridyl linker ligand in combination with $[Fe^{II}Pt^{II}(CN)_4]$ to form the material $[Fe(H_2O)_2Fe(DPSe)_2(Pt(CN)_4)_2]\cdot 3EtOH$ (DPSe = 4,4′-dipyridylselenide). Structural investigations reveal an unusual connectivity loosely resembling a 3D Hofmann topology where (1) there are two distinct local iron(II) environments, $[Fe^{II}N_6]$ (**Fe1**) and $[Fe^{II}N_4O_2]$ (**Fe2**), (2) as a consequence of axial water coordination to **Fe2**, there are "holes" in the $[Fe^{II}Pt^{II}(CN)_4]$ 4,4 sheets because of some of the cyanido ligands being terminal rather than bridging, and (3) bridging of adjacent sheets occurs only through one in two DPSe ligands, with the other acting as a terminal ligand binding through only one pyridyl group. The magnetic properties are defined by this unusual topology such that only **Fe1** is in the appropriate environment for a high-spin to low-spin transition to occur. Magnetic susceptibility data reveal a complete and abrupt hysteretic spin transition ($T_{1/2}\downarrow$ = 120 K and $T_{1/2}\uparrow$ = 130 K) of this iron(II) site; **Fe2** remains high-spin. This material additionally exhibits a photomagnetic response (uncommon for Hofmann-related materials), showing light-induced excited spin-state trapping [LIESST; T(LIESST) = 61 K] with associated bistability evidenced in a hysteresis loop ($T_{1/2}\downarrow$ = 60 K and $T_{1/2}\uparrow$ = 66 K).

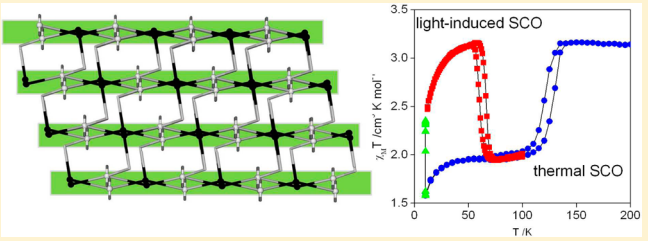

INTRODUCTION

Bimetallic Hofmann-type spin-crossover (SCO) systems are excellent examples of hybrid porous magnetic materials. Since their initiation in 1996, when Kitazawa et al. reported the 2D SCO compound $[Fe^{II}(pyridine)_2Ni^{II}(CN)_4]$,[1] a growing family of 2D and 3D Hofmann-type SCO systems have been reported, generally of the formula $[Fe^{II}(L)_nM^{II}(CN)_4]\cdot$guest ($n$ = 2 for unidentate ligands and n = 1 for bis-unidentate ligands; M^{II} = Ni, Pd, Pt).[2−12] These materials are comprised of bimetallic layers of the type $[Fe^{II}M^{II}(CN)_4]$, pillared (in the case of bispyridyl ligands) or separated (in the case of terminal ligands) to form 3D or 2D porous materials, respectively (Figure 1a−c). A vast variety of resultant materials are thus possible considering the variants of M^{II} and ligand, making these materials excellent candidates for systematic studies. In particular, the chemistry of Hofmann-type materials applied to the design of new iron(II) SCO frameworks is rapidly proving to be a compelling combination because these new materials typically demonstrate high degrees of connectivity, structural stability, and cooperativity and enhanced chemo-responsive functionality manifested in a variety of abrupt, hysteretic, and multistable thermo-, piezo-, photo-, and chemoinduced spin transitions. Above and beyond the impressive SCO attributes, 3D nanoporous Hofmann-type systems are revealing exceptional host−guest chemistries, in which significant structure/magnetism/guest-induced correlations are associated with the dynamic interplay between these properties.

The most widely studied system to date, [Fe(pyrazine)-$M^{II}(CN)_4]\cdot$guest (M^{II} = Pt, Pd, Ni), displays a highly cooperative and abrupt spin transition that is guest-responsive and can be fine-tuned toward room temperature.[3,7,8,13,14] The bistable temperature region appears to be influenced by the guest type and size, guest docking sites within the pore volume, and internal guest-pressure effects on the spin-state energetics. This reveals a complex relationship between the guest-induced spin transition, lattice dynamics, and novel memory capabilities. Variations in the preparative methods have enabled the fabrication of these molecular materials as thin films,[6,15,16] nanoparticles,[17] and nanocrystals[17,18] or their attachment onto gold surfaces,[15] demonstrating the feasible incorporation of these materials into existing and new commercial and industrial applications. It is widely demonstrated that the topology and

Received: February 27, 2014
Published: July 21, 2014

   dx.doi.org/10.1021/ic500323r | Inorg. Chem. 2014, 53, 7886−7893

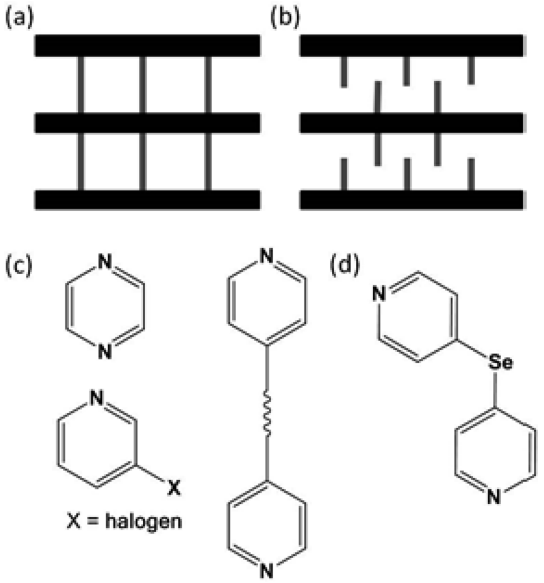

Figure 1. Schematic representation of the $[Fe^{II}M^{II}(CN)_4]$ (M^{II} = Pt, Pd, Ni) layers and interlayer spacing in (a) 3D and (b) 2D Hofmann-type materials. (c) Pyridyl-based ligands utilized in 2D and 3D Hofmann materials (bispyridyl examples include alkyl and aromatic spacers). (d) Bent ligand DPSe.

functional properties of coordination framework materials are principally directed by the chemistry and structure of their incorporated bridging ligands. A number of rigid, short, and linear bis-unidentate ligands (pyridine and its derivatives, pyrazine, pyrimidine, 4,4′-bipyridine, 4,4′-bis(pyridylethylene), and 4,4′-azopyridine, etc.)[1,6,7,11,12,19] have been incorporated into Hofmann-type SCO materials.

The strategic approach that we have taken here has been to incorporate a flexible and, in particular, nonlinear 4,4′-bispyridine ligand analogue (Figure 1d). The ligand used, 4,4′-dipyridylselenide (DPSe), additionally contains a chalcogen-based bridging component for which there are few bispyridine compounds of this kind found in the literature[4,20−25] and for which interest in their use has been directed mostly toward nonlinear-optical properties,[26,27] biological applications,[28,29] or exploration of the topologies of the few resulting compounds.[20,30,31] Consequently, this type of ligand remains largely unexplored in the field of coordination chemistry and SCO Hofmann-type materials. While the general topology that can be expected when linear (or approximately linear) bis- or monopyridyl ligands are incorporated into Hofmann materials is clear, the outcome of utilizing a bent bispyridyl ligand is less clear (Figure 1).[32] Indeed, here we find that the nonlinear nature of DPSe inhibits the formation of a traditional pillared-layer material, driving a distinct deviation from regular 3D Hofmann-type topology. This results in rare magnetic properties for the 3D Hofmann system, including quantitative light-induced excited spin-state trapping (LIESST)[4,6,33] and light-induced thermal hysteresis (LITH).

EXPERIMENTAL SECTION

Synthesis. The ligand 4,4′-dipyridylselenide (DPSe) was synthesized according to a previously reported method.[34] Well-formed yellow rectangular-prism single crystals of $[Fe(H_2O)_2Fe(DPSe)_2(M(CN)_4)_2]\cdot 3EtOH$ were obtained within 3 weeks by the slow diffusion of iron(II) perchlorate salt with $K_2[Pt(CN)_4]$ and ligand DPSe (molar ratio of 1:1:1) in a water−ethanol solvent mixture (1:1). ***Caution!*** *Iron(II) perchlorate salt is potentially explosive and must be handled with care.*

X-ray Crystallography. Data were collected on a Bruker-Nonius FR591 Kappa APEX-II diffractometer (Mo Kα radiation, λ = 0.71073 Å) equipped with an Oxford Cryosystems nitrogen gas cryosystem. Single crystals were attached with a film of perfluoropolyether oil to a mohair fiber mounted on a copper pin and data collected at 90 and 230 K. Diffraction data structural analyses were performed using *SAINT+* within the *APEX2* software suite.[35] Empirical absorption corrections were applied to all data using the *SADABS* program.[36] Solutions were obtained by direct methods using *SHELXS-97*[37] and refined with *SHELXL-2013*.[38] Non-hydrogen framework atoms were refined anisotropically, and hydrogen atoms were affixed using the riding model.

Thermal- and Light-Induced Magnetic Susceptibility. Magnetic susceptibility data were collected using a Quantum Design MPMS 5 SQUID magnetometer under an applied field of 1 T. The field was varied to check for any ferromagnetic impurities, and none were found. All measurements were performed on uniform crystalline samples in the temperature range 4−300 K, first upon cooling and then warming. To ensure that no loss of solvent occurred, the sample was held in a quartz tube with a very small amount of ethanol−water present. To prevent the damp sample from moving up the tube, care was taken to avoid a rapid temperature change. The thermal hysteresis region was measured using a rate of change of temperature of 2 K min^{-1}, with stabilization of the temperature at each data point for 1 min. Diamagnetic corrections were made for the quartz tube and for the ligands, the latter by means of Pascal's constants. An accurate value of $\chi_M T$ was found by measuring a dry polycrystalline sample at 295 K.[39−42]

Photomagnetic measurements were performed using a Kr^+ laser coupled via an optical fiber to the cavity of a MPMS-55 Quantum Design SQUID magnetometer operating at 2 T. A crystalline sample of the compound was suspended in silicone grease to inhibit desorption and then prepared in a thin layer (∼0.1 mg) to promote full penetration of the irradiated light. The sample mass was obtained by comparison with the thermal spin-transition curve measured on a larger accurately weighed polycrystalline sample.[39−42] Solvent desorption from the materials was further minimized by rapid sample mounting and minimal purging of the SQUID airlock. The sample was first slowly cooled to 10 K, ensuring that the potential trapping of high-spin (HS) species at low temperatures did not occur. Irradiation to photosaturation was carried out at 514.5 nm, and the power of the sample surface was adjusted to 5 mW cm^{-2}. Once photosaturation was reached (i.e., once $\chi_M T$ stopped increasing), irradiation was ceased and the temperature increased at a rate of 0.3 K min^{-1} to 100 K, and the magnetization was measured every 1 K to determine the T(LIESST) value, given by the extremeness of the $\delta\chi_M T/\delta T$ versus T curve for relaxation. The T(LIESST) value describes the limiting temperature above which the light-induced magnetic high-spin information is erased in a SQUID cavity.[39−42] In the absence of irradiation, the magnetism was also measured over the temperature range 10−300 K to follow the thermal spin transition and to obtain a low-temperature baseline.

LITH studies were performed by first attaining complete photosaturation by irradiation of the sample at 10 K and then maintaining irradiation while ramping the sample through the temperature profile of 10−100−10 K at a rate of 0.3 K min^{-1}.[41,43]

Thermal-induced spin-state-trapping (TIESST) measurements were performed by quench-cooling a sample at 10 K in the SQUID cavity (in the absence of irradiation) and then increasing the temperature to 100 K at a rate of 0.4 K min^{-1} to determine the T(TIESST) value, which is given by the minimum of the $\delta\chi_M T/\delta T$ versus T relaxation curve.

Relaxation kinetics of the metastable light-induced HS state were followed by irradiating the sample at 10 K until photosaturation was reached and then, while under constant irradiation, warming to a series of temperatures (40, 46, 50, 58, 60, 62, 64, and 66 K). At each temperature, the laser was turned off and the decay of the

dx.doi.org/10.1021/ic500323r | Inorg. Chem. 2014, 53, 7886−7893

Table 1. Single-Crystal Diffraction and Data Analysis

temperature/K	230(2)	90(2)
cryst color	yellow	dark red
spin state	HS	LS
formula	$[Fe(H_2O)_2Fe(DPSe)_2(Pt(CN)_4)_2]\cdot 3EtOH$ ($C_{34}H_{38}Fe_2N_{12}O_5Pt_2Se_2$)	$[Fe(H_2O)_2Fe(DPSe)_2(Pt(CN)_4)_2]\cdot 3EtOH$ ($C_{34}H_{38}Fe_2N_{12}O_5Pt_2Se_2$)
fw/g mol^{-1}	1354.54	1354.54
cryst syst	triclinic	triclinic
space group	$P\bar{1}$	$P\bar{1}$
a/Å	11.3127(18)	10.9555(11)
b/Å	14.687(2)	14.7173(14)
c/Å	14.767(2)	14.4397(15)
α/deg	85.881(8)	85.062(5)
β/deg	79.811(8)	78.378(5)
γ/deg	70.300(8)	69.983(5)
V/Å^3	2273.3(6)	2142.3(4)
Z	2	2
ρ_{calcd}/Mg m^{-3}	1.973	2.094
no. of data	17141	10613
no. of restraints/param	3/465	13/465
$R(F)$ $[I > 2\sigma(I)]$	0.0469	0.0362
$R(F)$ (all data)	0.0611	0.0686
$R_w(F^2)$ $[I > 2\sigma(I)]$	0.1180	0.0789
$R_w(F^2)$ (all data)	0.1240	0.0928
GOF	1.204	1.063

magnetization signal was followed for several hours or until relaxation back to the low-spin (LS) baseline was reached.

Optical Reflectivity. Optical reflectivity measurements were carried out using a custom-built reflectivity setup coupled with a CVI spectrometer. Reflectivity spectra within the range 450−900 nm and the temperature dependence of the signal at selected wavelengths (647 and 843 nm) were simultaneously recorded. The source of white light consisted of a halogen lamp emitting between 400 and 900 nm. The analyses were performed directly at the surface of thin layers of crystalline samples without any dispersion in a matrix. The crystalline sample was loaded with a small amount of guest solvent and quench-cooled to 270 K to prevent sample desolvation.

RESULTS AND DISCUSSION

Synthesis and Characterization. Single crystals were prepared via slow diffusion techniques, and the composition was investigated using single-crystal X-ray diffraction analysis and Raman spectroscopy. Raman spectra revealed characteristic cyanido stretching vibrational modes: a strong doublet at 2198 and 2178 cm^{-1}, corresponding to bound cyanide (Pt−C≡N−Fe), and a weak doublet shifted to lower wavenumbers centered at 2159 cm^{-1}, which corresponds to the terminating (uncoordinated Pt−C≡N) cyanide units. The collection of meaningful powder X-ray diffraction data was not possible because significant loss of crystallinity resulted even when the sample was carefully pulverized.

X-ray Crystallography. Single-crystal X-ray diffraction structure and refinement details are given in Table 1. Selected bond lengths and structural parameters are given in Table S1 in the Supporting Information (SI). Variable-temperature single-crystal analysis was carried out at 230 K (HS) and 90 K (LS) to assess the structural changes associated with the spin transition. The 230 and 90 K crystal structures exhibit characteristic HS and LS **Fe1**−N bond distances [the average Fe1−N distances are 2.179 Å (230 K) and 1.969 Å (90 K)], respectively. These changes in the **Fe1**−N distances consequential to SCO confer a significant decrease in the crystal volume of 5.76% between the structures of the HS state at 230 K and the LS state at 90 K. The **Fe2** bond lengths remain in the HS state at both temperatures (Table S1 in the SI).

At both temperatures, there are two crystallographically distinct iron(II) sites in this material, each with distinct coordination environments (Figure 2a,b). The **Fe1** site resembles a typical SCO [$Fe^{II}N_6$] chromophore, axially coordinated to DPSe ligands (one bridging and terminating) and equatorially bound to four cyanide units (one containing a terminal cyanide group). The **Fe2** coordination sphere is an uncommon SCO-type [$Fe^{II}N_4O_2$] chromophore[44] comprised of axially coordinated water molecules, three equatorially bound nitrogen-donating cyanide units, and one equatorial DPSe ligand.

The complete 3D framework, which resembles a disrupted 3D Hofmann-type SCO material, consists of layers of [**Fe2**$(H_2O)_2$**Fe1**$(M(CN)_4)_2$] undulating grids that contain rectangular "holes" generated by the terminal cyanide units and filled by DPSe ligands bound equatorially to the **Fe2** sites (Figure 2c). The **Fe1** and **Fe2** sites alternate in rows within the layer, and hydrogen-bonding interactions are present between the terminal cyanide group and the bound water molecules (Figure 2c). The layers are nonplanar because of the octahedral out-of-plane tilt of the **Fe2** atoms, likely influenced by the steric requirements of the equatorially bound DPSe groups (Figures 2d and 3). The 3D connectivity is completed by coordination of the **Fe1** and **Fe2** sites via bent, bridging DPSe ligands that orient in an alternating up and down fashion with respect to adjacent **Fe2** sites (Figure 3).

Of importance to the magnetic properties, the rows of **Fe1** SCO-active atom sites are completely interconnected through the cyanide linkage (adjacent rhomboid Fe1−Fe1 distances of 7.214(2) and 7.691(2) Å along the row), while rows of **Fe2** sites are disjointed with respect to the cyanide linkage due to "holes" in the 4,4-grid layer (the closest adjacent Fe2−Fe2 distances are 7.332(2) and 8.346(2) Å; Figure 3). The axially bound water group has a short hydrogen-bonding interaction with the terminating cyanide unit and also with the pyridyl

dx.doi.org/10.1021/ic500323r | Inorg. Chem. 2014, 53, 7886−7893

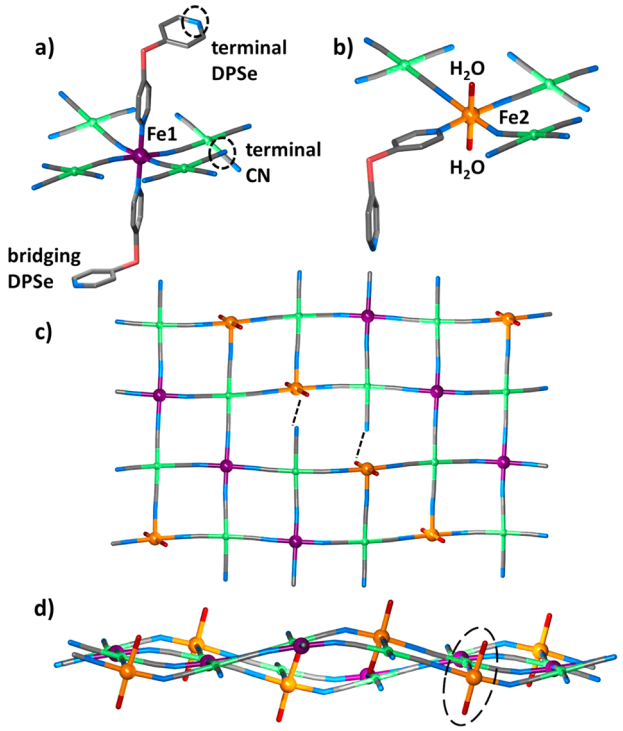

Figure 2. Structural representations of the distinct coordination environment around (a) **Fe1** and (b) **Fe2** with terminal and bridging units indicated. (c and d) Single undulating layer illustrating the bridging and terminal $[Pt(CN)_4]^{2-}$ components, the distribution of **Fe1** and **Fe2** sites within the grid, interlayer hydrogen-bonding interactions, and **Fe1** octahedral tilt.

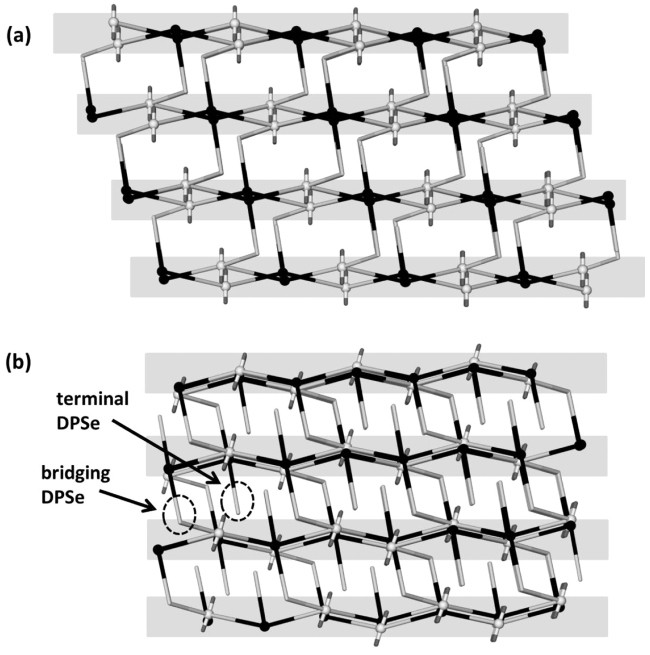

Figure 3. (a and b) Two structural topological representations of relative 90° rotation about the *c* axis. The terminal and bridging DPSe sites are highlighted in part b. The general 2D-layer (gray box) positioning and arrangement of **Fe1** (dark spheres) and **Fe2** (light spheres) are shown.

nitrogen of the terminating DPSe ligand (Figure S2 and Table S1 in the SI).

The framework houses 1D channels that account for 26.8%[45] of the total crystal volume (Figure S3 in the SI), filled with solvent molecules. Host−guest interactions are present between the axially bound water group and two of the guest ethanol molecules (Figure S2 and Table S1 in the SI).

Thermal- and Light-Induced Magnetic Susceptibility. Temperature-dependent magnetic susceptibility measurements for a crystalline sample were conducted to follow the iron(II) spin-state changes (Figure 4). From room temperature to 110

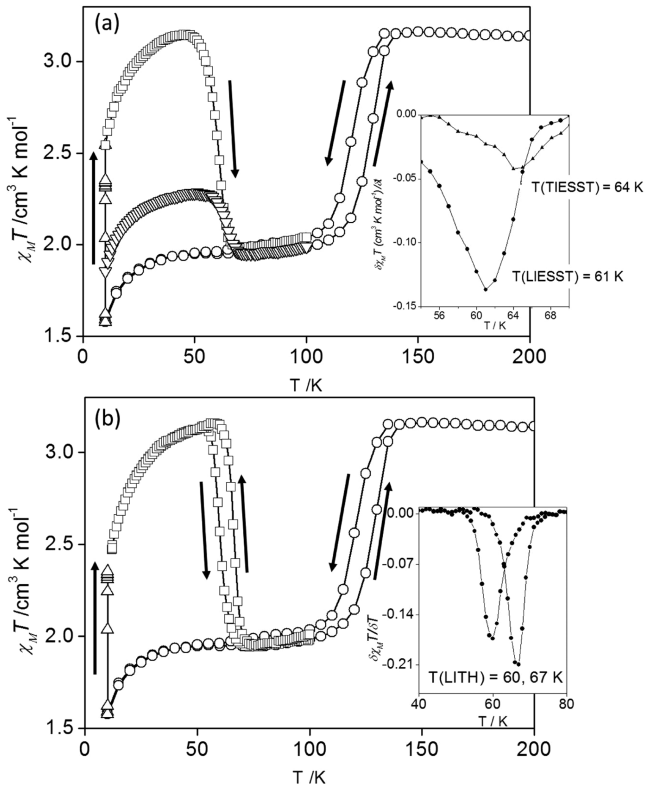

Figure 4. Plots of $\chi_M T$ versus temperature over the range 10−200 K for the thermal- (○) and light-induced SCO. (a) Quench cooling (10 K) followed by warming to 100 K (▽), under irradiation at 10 K (λ = 514.5 nm, △), and after irradiation in the dark to 100 K (□). Inset: derivative of $\chi_M T$, with minima indicating T(LIESST) and T(TIESST) values. (b) Under constant irradiation over the range 10−100−10 K (□). Inset: derivative of $\chi_M T$, with minima indicating T(LITH) values.

K, the $\chi_M T$ product remains approximately constant at 3.25 cm^3 K mol^{-1}, indicative of all iron(II) sites existing in the HS state. Upon further cooling, an abrupt drop in $\chi_M T$ is observed, reaching a value of ca. 1.9 cm^3 K mol^{-1} at 90 K. This value is in the region expected for an approximate 50% spin transition, suggesting that only half of the available iron(II) sites crossover from the HS state to the LS state. This is as expected from structural analysis. The decrease in $\chi_M T$ observed below ∼30 K, reaching ∼1.6 cm^3 K mol^{-1} at 10 K, is likely due to zero-field splitting (ZFS) of the HS state, possibly with a weak Fe···Fe antiferromagnetic coupling contribution, but not to a low-temperature HS-to-LS spin transition. Further support for ZFS is given below.

With heating of the sample, a marked 10 K hysteresis is revealed. The critical transition temperatures are $T_{1/2}\downarrow$ = 120 K and $T_{1/2}\uparrow$ = 130 K, which define the temperature range of thermal bistability. The abrupt spin transition and hysteresis

dx.doi.org/10.1021/ic500323r | Inorg. Chem. 2014, 53, 7886−7893

indicate strong cooperativity between the SCO-active iron(II) centers, as is often observed in Hofmann-type materials.

With quench cooling to 10 K, some trapping of HS species is observed (Figure 4a). Upon heating from 10 K, the $\chi_M T$ product of the metastable HS state increases, attaining a maximum value of 2.82 cm^3 K mol^{-1} at 49 K, indicative of a thermally induced trapping yield of ~25% (of SCO-active sites). Heating beyond 49 K sees the thermally trapped HS species relax to the LS state by 80 K. The value at which the thermally trapped stored information is erased, T(TIESST) (defined as the minimum of the differential $\delta\chi_M T/\delta T$ when the temperature is increased from 10 K at a rate of 0.4 K min^{-1} inside a SQUID cavity), is 64 K (Figure 4a, inset).[44]

Detailed photomagnetic studies revealed that with irradiation at 10 K a photoexcitation of the LS species to a metastable HS state is observed as a sharp increase in the $\chi_M T$ product, reaching saturation at 2.54 cm^3 K mol^{-1}. Near-complete photoconversion of the SCO-active iron(II) sites to the metastable HS state is observed, consistent with the spectroscopic data (Figure 4a). In the absence of irradiation, the $\chi_M T$ values increase further upon heating to a maximum $\chi_M T$ value of 3.15 cm^3 K mol^{-1} at ca. 50 K, thereby reflecting the quantitative trapping of metastable species. This increase in $\chi_M T$ mirrors that seen over the same temperature range in the thermal spin transition and is attributed to the ZFS of the iron(II) HS state in nonperfect octahedral surroundings. The value at which the photoinduced trapped information is erased, T(LIESST), is 61 K (Figure 4a, inset).[39] The difference in the T(TIESST) and T(LIESST) values (3 K) is consistent with that of previously reported SCO frameworks[45] and is attributable to different experimental conditions and underlying deviations in the fundamental properties of the respective processes.[46]

The photoexcitation process was monitored under constant irradiation to assess the presence of LITH.[41] Figure 4b shows the cooling and heating data over the range 100−10−100 K in the presence of constant irradiation (λ = 514.5 nm). A hysteresis of ca. 6 K is observed, demonstrating the existence of a photoinduced bistability. The LITH transition temperatures are found to be $T_{1/2}\downarrow$ = 60 K and $T_{1/2}\uparrow$ = 66 K. The presence of LITH is ascribed to a degree of cooperativity that exists between the SCO-active **Fe1** sites.[43,47,48] With cooling and warming under irradiation, two effects are operational: the light-induced trapping of the system in the metastable HS state, on the one hand, and the relaxation from this HS state toward the ground LS state, on the other hand. In the solid state, and principally in pure iron(II) compounds, the HS-to-LS relaxation is strongly influenced by cooperative effects.

Optical Reflectivity. Crystals display marked thermochromism associated with SCO behavior, converting reversibly from yellow at room temperature to dark red at liquid-nitrogen temperature because of the presence of the spin-allowed $^1A_1 \rightarrow {}^1T_1$ d−d transition and increased intensity of the metal-to-ligand charge-transfer (MLCT) band in the LS state.

The TIESST and LIESST effects were monitored by simultaneously recording the thermal evolution of the diffuse absorption spectra (400−900 nm) and the reflectivity signals at 647 and 843 nm under constant white-light irradiation over the temperature range 250−10−250 K (Figure 5).

Upon cooling from 140 to 70 K, the absorption band intensity at 800−900 nm [which is characteristic of the d−d transitions of the HS iron(II) state] decreases markedly and, concomitantly, the absorption band at about 600 nm (assigned

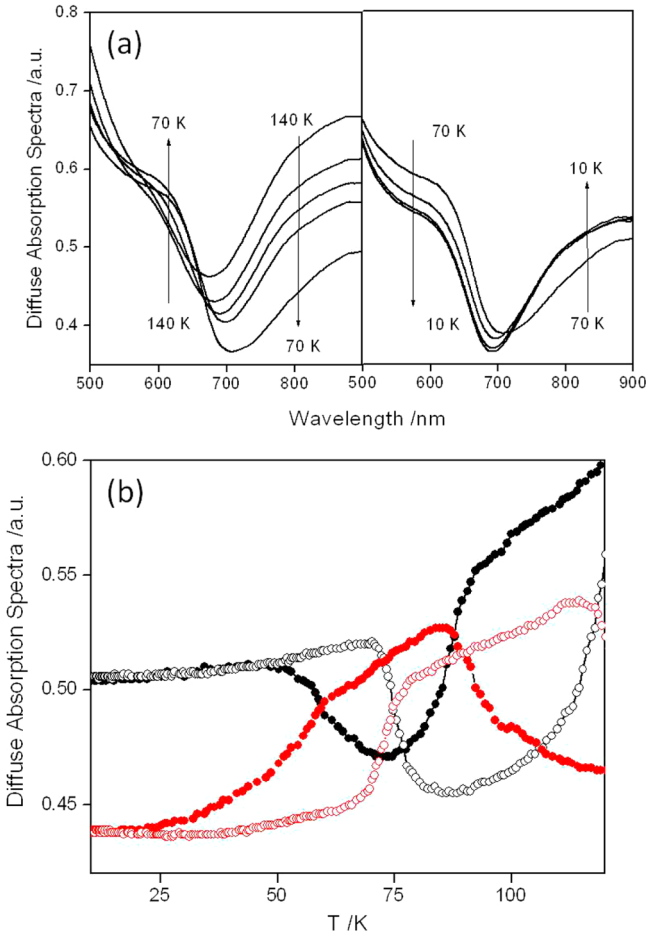

Figure 5. (a) Thermal evolution of the diffuse absorbance spectra under light irradiation over the ranges 140−70 K (left, thermal SCO) and 70−10 K (right, LIESST). (b) Temperature dependence of the absorbances at 647 nm (red) and 843 nm (black) for the cooling (closed circles) and warming (open circles) modes under light irradiation.

to both d−d and MLCT transitions of the LS state) increases. Over the range 70−10 K, the LIESST and LITH effects are observed. The thermal dependence of the relative absorbance signals at 647 and 843 nm further highlight these features; the 140−70 K region resembles the magnetic properties of a hysteretic spin transition, while cooling below 70 K suggests near-quantitative LIESST (Figure 5b).

LIESST Relaxation Kinetics. The dynamics of the LIESST relaxation of the metastable HS molar fraction, γ_{HS}, following photosaturation (in the absence of irradiation) were investigated in the 40−66 K temperature range where the HS−LS state relaxation is thermally activated (Figure 6). Values for γ_{HS} were deduced from the equation $[(\chi_M T)_{h\nu} - (\chi_M T)_{LS}]/[(\chi_M T)_{HS} - (\chi_M T)_{LS}]$ where $(\chi_M T)_{h\nu}$ is the magnetic value reached after irradiation, $(\chi_M T)_{LS}$ is the magnetic value corresponding to the fully ground state LS **Fe1** sites, and $(\chi_M T)_{HS}$ is the high-temperature magnetic value corresponding to entirely HS **Fe1** sites. The relaxation behavior strongly deviates from a single-exponential behavior and exhibits a rapid initial decay followed by a long tail of a much slower decay process, representative of a stretched exponential behavior.[49] To reproduce this type of curve, Hauser et al.[50] used a distribution of relaxation rates k_{HL}, where at a given temperature k_{HL} can be obtained by using a Gaussian

dx.doi.org/10.1021/ic500323r | Inorg. Chem. 2014, 53, 7886−7893

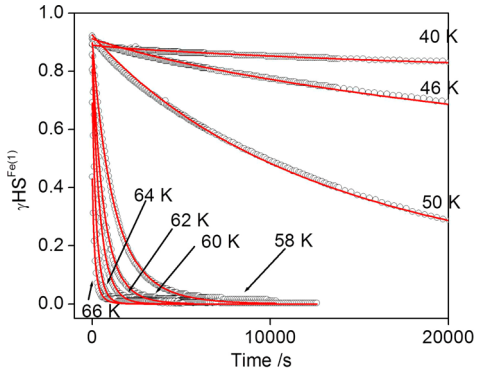

Figure 6. Metastable HS-to-LS relaxation kinetics. Time dependence at various temperatures of the HS molar fraction generated by light irradiation at 10 K (○). The relaxation curves are fitted according to stretched exponential behavior; see the text.

distribution of activation energies (E_0) and a preexponential factor k_0:

$$\gamma_{HS} = \exp(-k_{HL}t) \quad (1)$$

Following this procedure, least-squares fitting of the relaxation curves using the stretched exponential model results in a satisfactory agreement, illustrated by the solid lines in Figure 6.

It is well established that the HS → LS relaxation after LIESST for spin-transition compounds is usually strongly influenced by cooperative effects,[51] with systems that display strong cooperativity[52] being expected to display sigmoidal relaxation behavior associated with self-acceleration. Indeed, the abrupt thermal-, optical-, and light-induced hysteretic spin transitions exhibited by this material are archetypal properties representative of strong cooperative systems. Thus, the observed stretched exponential behavior is unexpected in this instance because it is more commonly associated with systems in which there is little or no lattice cooperativity.

At low temperatures (≤50 K), complete relaxation was not observed after 10 h. For instance, at 40 K the change in the HS fraction is only 22% after 16 h. This suggests that the relaxation process is governed by the quantum tunneling regime,[42] and an estimation of the rate constant $k_{HL}(T\rightarrow 0)$ is consequently unrealistic in view of the long lifetime. The HS → LS relaxation kinetics become considerably more rapid for temperatures above 50 K, indicating that relaxation at these higher temperatures is within the thermally activated region.

Figure S5 in the SI plots the logarithm of the rate constant, $\ln[k_{HL}(T)]$, as a function of the inverse temperature, determined from the stretched exponential fitting for each temperature within the thermally activated relaxation region ($T \geq 50$ K). An Arrhenius linear regression plot yields the apparent values for the activation energy, E_a (668 cm^{-1} for the HS → LS relaxation), and the preexponential factor, $k_{HL}(T\rightarrow\infty)$ (2.5×10^9 s^{-1}). In general, for LIESST relaxation studies, it is difficult to deduce the kinetic parameters of E_a and $k_{HL}(T\rightarrow\infty)$ that are involved in the thermally activated region because the true values would only be obtained at higher temperatures in the limit regime of thermal activation. Thus, the apparent kinetic parameters are often underestimated.[52,53] The activation energy value (668 cm^{-1}), which is linked to the degree of cooperativity, is of the correct magnitude for $Fe^{II}N_6$ SCO systems that exhibit moderate-to-weak cooperativity.[53,54] This is also reflected in the stretched exponential decay relaxation behavior. In contrast, the rate constant value is relatively high for such systems,[53−55] suggesting an underlying cooperative facet that is congruent with the abrupt hysteretic SCO properties of this material. Furthermore, the presence of the LITH effect, which is a process governed by a competition between constant photoexcitation and self-accelerated thermal relaxation, is attributed to cooperative photoexcitation mechanisms.[53] These results suggest that the photo- and thermomagnetic properties of this material comprise a combination of weak and strong cooperative components.

In assessing this anomalous behavior, we note first that the intrinsic nature of Hofmann-type SCO systems represents both strong and weak cooperative pathways, originating from the rigid $[Fe^{II}M^{II}CN_4]$ layers and flexible organic pillars, respectively. Second, the uniquely coordinated Hofmann-type layer in this system, containing both SCO-active (**Fe1**) and HS sites (**Fe2**), presents an example analogous to metal dilution. Indeed, detailed thermo- and photomagnetic studies on the metal dilution series $[Fe_xZn_{1-x}(bpp)_2](NCSe)_2$[56] revealed that cooperativity is diminished with increasing dilution. Significantly, this study revealed a trend from sigmoidal toward stretched exponential photomagnetic decay with increasing metal dilution, so this may account for the behavior observed here. Overall, a comprehensive rationalization of the overall photomagnetic behavior is not possible because there are few detailed reports on the LIESST, relaxation kinetics, and LITH properties of Hofmann-type materials. Further, such studies will be of fundamental importance for Hofmann systems because the intrinsic highly cooperative bimetallic layers linked into two or three dimensions by ligands prone to weak cooperativity present a unique situation. Here, the cooperative spin-transition behavior combined with a reduced thermal transition temperature enables the LIESST effect and thus provides a rare example toward a fundamental understanding.

CONCLUSIONS

By using a nontraditional type of bispyridyl ligand, we have generated an entirely new Hofmann-type topology, which has resulted in both thermal- and light-induced bistability. While many of the previously reported Hofmann materials show significant cooperativity in the form of thermal hysteresis, likely because of the communication provided by the short cyanido ligand bridges, there are few Hofmann-type materials that display light-induced activity. In contrast to thermal SCO, light-induced phenomena are metastable because of the competition between the thermal-trapping and quantum-tunneling effects, and thus the short cyanido bridges that provide a good path to thermal bistability may indeed be counteractive with respect to maintaining metastability in the presence of light. Here, we show that by disrupting the $[Fe^{II}Pt(CN)_4]$ grids but maintaining the 3D communication with bispyridyl ligand bridging and an extensive hydrogen-bonding network, both thermal- and light-induced bistability can be achieved.

In addition to providing a new synthetic avenue for exploring cooperative effects in SCO materials, the construction of structurally complex 3D networks of the type described raises new opportunities for exploring the interplay between reversible host−guest effects and SCO. Most notably, the incorporation of labile metal binding sites into SCO frameworks, such as the water-bound $[Fe^{II}N_4O_2]$ sites seen here, might potentially be exploited for specific guest binding toward guest-sensing applications, including as bare metal sites. This would be a new means to probing guest-sensitive SCO

dx.doi.org/10.1021/ic500323r | Inorg. Chem. 2014, 53, 7886−7893

properties in porous materials, with chemisorptive binding at metal sites, in principle, providing a considerably more selective interaction than the physisorptive host−guest interaction prevalent in other porous SCO systems. Moreover, strong directional binding at such sites is expected to have a profound steric and electronic influence on the proximal SCO centers, in principle leading to very high sensitivity of the electronic transition to guest adsorption and exchange.

■ ASSOCIATED CONTENT

Supporting Information

Further structural and magnetic data and CCDC 955805 and 955806 containing the supplementary crystallographic data for this paper. This material is available free of charge via the Internet at http://pubs.acs.org. The atomic coordinates have been deposited with the Cambridge Crystallographic Data Centre. The coordinates can be obtained, upon request, from the Director, Cambridge Crystallographic Data Centre, 12 Union Road, Cambridge CB2 1EZ, U.K.

■ AUTHOR INFORMATION

Corresponding Author

*E-mail: cameron.kepert@sydney.edu.au.

Notes

The authors declare no competing financial interest.

■ ACKNOWLEDGMENTS

The Australian Research Council is thanked for providing Discovery Grants and Research Fellowships to support this work at the University of Sydney and Monash University. Financial support for the photomagnetic LIESST work was kindly provided by a French−Australia FAST/DEST grant, and this allowed the Australian participants to travel to Bordeaux to carry out measurements. The authors also thank the Aquitaine Region for supporting the development of the international platform of photomagnetism.

■ REFERENCES

(1) Kitazawa, T.; Gomi, Y.; Takahashi, M.; Takeda, M.; Enomoto, M.; Miyazaki, A. *J. Mater. Chem.* **1996**, *6*, 119−121.
(2) Ohtani, R.; Arai, M.; Ohba, H.; Hori, A.; Takata, M.; Kitagawa, S.; Ohba, M. *Eur. J. Inorg. Chem.* **2013**, 738−744.
(3) Bao, X.; Shepherd, H. J.; Salmon, L.; Molnár, G.; Tong, M.-L.; Bousseksou, A. *Angew. Chem., Int. Ed.* **2013**, *52*, 1198−1202.
(4) Sciortino, N. F.; Scherl-Gruenwald, K. R.; Chastanet, G.; Halder, G. J.; Chapman, K. W.; Létard, J.-F.; Kepert, C. J. *Angew. Chem., Int. Ed.* **2012**, *51*, 10154−10158.
(5) Ohtani, R.; Yoneda, K.; Furukawa, S.; Horike, N.; Kitagawa, S.; Gaspar, A. B.; Muñoz, M. C.; Real, J. A.; Ohba, M. *J. Am. Chem. Soc.* **2011**, *133*, 8600−8605.
(6) Agustí, G.; Cobo, S.; Gaspar, A. B.; Molnár, G.; Moussa, N. O.; Szilágyi, P. Á.; Pálfi, V.; Vieu, C.; Muñoz, M. C.; Real, J. A.; Bousseksou, A. *Chem. Mater.* **2008**, *20*, 6721−6732.
(7) Niel, V.; Martinez-Agudo, J. M.; Muñoz, M. C.; Gaspar, A. B.; Real, J. A. *Inorg. Chem.* **2001**, *40*, 3838−3839.
(8) Southon, P. D.; Liu, L.; Fellows, E. A.; Price, D. J.; Halder, G. J.; Chapman, K. W.; Moubaraki, B.; Murray, K. S.; Létard, J.-F.; Kepert, C. J. *J. Am. Chem. Soc.* **2009**, *131*, 10998−11009.
(9) Halcrow, M. A. *Spin Crossover Materials: Properties and Applications*; John Wiley & Sons Ltd.: New York, 2013.
(10) Martínez, V.; Gaspar, A. B.; Muñoz, M. C.; Bukin, G. V.; Levchenko, G.; Real, J. A. *Chem.—Eur. J.* **2009**, *15*, 10960−10971.
(11) Muñoz, M. C.; Gaspar, A. B.; Galet, A.; Real, J. A. *Inorg. Chem.* **2007**, *46*, 8182−8192.
(12) Niel, V.; Muñoz, M. C.; Gaspar, A. B.; Galet, A.; Levchenko, G.; Real, J. A. *Chem.—Eur. J.* **2002**, *8*, 2446−2453.
(13) Larionova, J.; Salmon, L.; Guari, Y.; Tokarev, A.; Molvinger, K.; Molnár, G.; Bousseksou, A. *Angew. Chem., Int. Ed.* **2008**, *47*, 8236−8240.
(14) Rodríguez-Velamazán, J. A.; González, M. A.; Real, J. A.; Castro, M.; Muñoz, M. C.; Gaspar, A. B.; Ohtani, R.; Ohba, M.; Yoneda, K.; Hijikata, Y.; Yanai, N.; Mizuno, M.; Ando, H.; Kitagawa, S. *J. Am. Chem. Soc.* **2012**, *134*, 5083−5089.
(15) Molnár, G.; Cobo, S.; Real, J. A.; Carcenac, F.; Daran, E.; Vieu, C.; Bousseksou, A. *Adv. Mater.* **2007**, *19*, 2163−2167.
(16) Cobo, S.; Molnár, G.; Real, J. A.; Bousseksou, A. *Angew. Chem., Int. Ed.* **2006**, *45*, 5786−5789.
(17) Boldog, I.; Gaspar, A. B.; Martínez, V.; Pardo-Ibañez, P.; Ksenofontov, V.; Bhattacharjee, A.; Gütlich, P.; Real, J. A. *Angew. Chem., Int. Ed.* **2008**, *47*, 6433−6437.
(18) Volatron, F.; Catala, L.; Rivière, E.; Gloter, A.; Stéphan, O.; Mallah, T. *Inorg. Chem.* **2008**, *47*, 6584−6586.
(19) Ohba, M.; Yoneda, K.; Agustí, G.; Muñoz, M. C.; Gaspar, A. B.; Real, J. A.; Yamasaki, M.; Ando, H.; Nakao, Y.; Sakaki, S.; Kitagawa, S. *Angew. Chem., Int. Ed.* **2009**, *48*, 4767−4771.
(20) Jung, O.-S.; Park, S. H.; Kim, D. C.; Kim, K. M. *Inorg. Chem.* **1998**, *37*, 610−611.
(21) Marinho, M. V.; Yoshida, M. I.; Krambrock, K.; De Oliveira, L. F. C.; Diniz, R.; Machado, F. C. *J. Mol. Struct.* **2009**, *923*, 60−66.
(22) Ni, Z.; Vittal, J. J. *Cryst. Growth Des.* **2001**, *1*, 195−197.
(23) Xie, Y.-B.; Bu, X.-H. *J. Cluster Sci.* **2003**, *14*, 471−482.
(24) Xie, Y.-B.; Li, J.-R.; Zhang, C.; Bu, X.-H. *Cryst. Growth Des.* **2005**, *5*, 1743−1749.
(25) Su, X.-C.; Guo, Y.-h.; Zhu, S.-R.; Lin, H.-K. *J. Mol. Struct.* **2002**, *643*, 147−153.
(26) Niu, Y.; Li, Z.; Song, Y.; Tang, M.; Wu, B.; Xin, X. *J. Solid State Chem.* **2006**, *179*, 4003−4010.
(27) Xu, Q.-F.; Zhou, Q.-X.; Lu, J.-M.; Xia, X.-W.; Wang, L.-H.; Zhang, Y. *Polyhedron* **2007**, *26*, 4849−4859.
(28) Zhao, G. H.; Hu, X. S.; Yu, P.; Lin, H. K. *Transition Met. Chem.* **2004**, *29*, 607−612.
(29) Zhao, G. H.; Lin, H. K.; Zhu, S. R.; Sun, H. W.; Chen, Y. Y. *Anti-Cancer Drug Des.* **1998**, *13*, 769−777.
(30) Lu, J. F.; Xu, Q. F.; Zhou, Q. X.; Wang, Z. L.; Lu, J. M.; Xia, X. W.; Wang, L. H.; Zhang, Y. *Inorg. Chim. Acta* **2009**, *362*, 3401−3406.
(31) Jung, O. S.; Park, S. H.; Lee, Y. A.; Lee, U. *Chem. Lett.* **2000**, 1012−1013.
(32) Muñoz-Lara, F. J.; Gaspar, A. B.; Muñoz, M. C.; Ksenofontov, V.; Real, J. A. *Inorg. Chem.* **2012**, *52*, 3−5.
(33) Martinez, V.; Castillo, Z. A.; Muñoz, M. C.; Gaspar, A. B.; Etrillard, C.; Létard, J.-F.; Terekhov, S. A.; Bukin, G. V.; Levchenko, G.; Real, J. A. *Eur. J. Inorg. Chem.* **2013**, *5*−*6*, 813−818.
(34) Boduszek, B.; Wieczorek, J. S. *Polym. J. Chem.* **1983**, *57*, 641−643.
(35) *APEX 2 software suite*; Bruker Analytical X-ray Instruments Inc.: Madison, WI, 2005.
(36) Sheldrick, G. M. *SADABS. Empirical Absorption Correction Program for Area Detector Data*; University of Göttingen: Göttingen, Germany, 1996.
(37) Sheldrick, G. M. *SHELXS97*; University of Göttingen: Göttingen, Germany, 1997.
(38) Sheldrick, G. M. *SHELXL97*, version 2013; University of Göttingen: Göttingen, Germany, 1997.
(39) Létard, J.-F. *J. Mater. Chem.* **2006**, *16*, 2550−2559.
(40) Létard, J.-F.; Guionneau, P.; Nguyen, O.; Costa, J. S.; Marcen, S.; Chastanet, G.; Marchivie, M.; Goux-Capes, L. *Chem.—Eur. J.* **2005**, *11*, 4582−4589.
(41) Létard, J.-F.; Guionneau, P.; Rabardel, L.; Howard, J. A. K.; Goeta, A. E.; Chasseau, D.; Kahn, O. *Inorg. Chem.* **1998**, *37*, 4432−4441.
(42) Hauser, A. *Top. Curr. Chem.* **2004**, *234*, 155−198.
(43) Hauser, A. *Chem. Phys. Lett.* **1992**, *192*, 65−70.

(44) Paradis, N.; Chastanet, G.; Létard, J.-F. *Eur. J. Inorg. Chem.* **2012**, 3618−3624.
(45) Halder, G. J.; Chapman, K. W.; Neville, S. M.; Moubaraki, B.; Murray, K. S.; Létard, J.-F.; Kepert, C. J. *J. Am. Chem. Soc.* **2008**, *130*, 17552−17562.
(46) Bauer, W.; Scherer, W.; Altmannshofer, S.; Weber, B. *Eur. J. Inorg. Chem.* **2011**, 2803−2818.
(47) Romstedt, H.; Hauser, A.; Spiering, J. *J. Phys. Chem. Solids* **1998**, *59*, 265−275.
(48) Desaix, A.; Roubeau, O.; Jeftic, J.; Haasnoot, J. G.; Boukheddaden, K.; Codjovi, E.; Linares, J.; Nogues, M.; Varret, F. *Eur. Phys. J. B* **1998**, *6*, 183−193.
(49) Capes, L.; Létard, J.-F.; Kahn, O. *Chem.—Eur. J.* **2000**, *6*, 2246−2255.
(50) Hauser, A.; Adler, J.; Gütlich, P. *Chem. Phys. Lett.* **1988**, *152*, 468−472.
(51) Hinek, R.; Spiering, H.; Schollmeyer, D.; Gütlich, P.; Hauser, A. *Chem.—Eur. J.* **1996**, *2*, 1427−1434.
(52) Hauser, A.; Jeftic, J.; Romstedt, H.; Hinek, R.; Spiering, H. *Coord. Chem. Rev.* **1999**, *190−192*, 471−491.
(53) Létard, J. F.; Chastanet, G.; Nguyen, O.; Marcen, S.; Marchivie, M.; Guionneau, P.; Chasseau, D.; Gütlich, P. *Monatsh. Chem.* **2003**, *134*, 165−182.
(54) Capes, L.; Létard, J. F.; Kahn, O. *Chem.—Eur. J.* **2000**, *6* (12), 2246−2255.
(55) Carbonera, C.; Costa, J. S.; Money, V. A.; Elhaïk, J.; Howard, J. A. K.; Halcrow, M. A.; Létard, J.-F. *Dalton Trans.* **2006**, *25*, 3058−3066.
(56) Baldé, C.; Desplanches, C.; Le Gac, F.; Guionneau, P.; Létard, J.-F. *Dalton Trans.* **2014**, *43*, 7820−7829.